sustainability

MDPI

Article

Numerical and Economic Analysis of Hydronic-Heated Anti-Icing Solutions on Underground Park Driveways

Nurullah Kayaci [1,2] and Baris Burak Kanbur [3,*]

[1] Department of Mechanical Engineering, Yildiz Technical University, 34349 Istanbul, Turkey
[2] Department of Mechanical Engineering, Tekirdag Namik Kemal University, 59860 Tekirdag, Turkey
[3] Department of Civil and Mechanical Engineering, Technical University of Denmark, 2800 Kongens Lyngby, Denmark
* Correspondence: babukan@dtu.dk

Abstract: Snow and ice forming on the entrance and exit driveways of underground car parks of buildings brings serious difficulties and risks in safe parking for vehicles in winter. Even though traditional methods such as chemical salt and snow plowing reduce slippery conditions on driveways, they also result in infrastructure- and environment-related damages. Hydronic heating is an alternative way to prevent snow and ice forming; thereby, the hydronic heating driveway (HHD) is a promising technique for energy-efficient and environment-friendly solutions. This study presents a time-dependent three-dimensional numerical heat transfer model for HHD applications with realistic boundary conditions and meteorological data in the MATLAB environment. After developing the numerical heat transfer model, the model is applied to a case study in Istanbul, Turkey and followed by an economic comparison with the commercial electrically-heated driveways (EHD) method that is applied in two different ways; applying the electric cables in (i) whole driveway and (ii) only tire tracks. Different escalation rates in natural gas and electricity, hot fluid inlet temperature, air temperature, and the number of parallel pipes are the main parameters in the case study. Results show that the decrease in pipe spacing drops the investment cost term but it needs a higher supplied fluid temperature for anti-icing, and therefore the operating cost term increases. Among other cases was the number of parallel pipes, with 50 being the most economically feasible solution for all air temperatures ranging from 0 °C to −10 °C. The economic comparison shows that the EHD with only tire tracks has the minimum total cost as it significantly decreased both the operating and investment cost terms. In case of an anti-icing requirement on the whole road surface, the HHD system was found to be preferable to the EHD whole driveway scenario at air temperatures of 0 °C and −5 °C, while it is more beneficial only for the high electricity escalation rates at the ambient temperature of −10 °C.

Keywords: numerical heat transfer; ground heat exchanger; anti-icing; hydronic heating; electric heating; economic analysis; green building; underground parking

Citation: Kayaci, N.; Kanbur, B.B. Numerical and Economic Analysis of Hydronic-Heated Anti-Icing Solutions on Underground Park Driveways. *Sustainability* **2023**, *15*, 2564. https://doi.org/10.3390/su15032564

Academic Editors: Rosolino Vaiana and Vincenzo Gallelli

Received: 21 December 2022
Revised: 20 January 2023
Accepted: 29 January 2023
Published: 31 January 2023

1. Introduction

Snow and ice formation on driveways in winter results in serious risky situations and safety concerns that also cause serious delays and cost drawbacks in daily life [1–4]. From past to present, many studies focused on economically viable snow and ice removal methods for densely populated areas (e.g., overpopulated living areas), public areas (e.g., hospitals, municipal buildings), and transport infrastructure (e.g., airports) as explained in detail by recent critical review studies [5–9]. In general, these methods can be divided into two types: passive and active. One of the most-preferred passive methods is applying salt or some other chemicals on the target surface to prevent snow and ice forming as the method decreases the freezing point of water [10]. Increasing the surface slippery resistance is also a passive way by applying sand or gravel materials to the target road surfaces; hereby, the surface friction is strengthened. While these methods are easy-to-apply

and very wide in different regions, they raise environmental concerns due to penetrating vegetation, soil, and groundwater [11,12]. Another passive approach is snow plowing but it is both time- and energy-consuming while causing additional physical damage to the roads [13,14]. Apart from the passive solutions, hydronic heated driveways (HHD) and electrically heated driveways (EHD) are active solutions to remove snow or prevent icing on the road surfaces by (i) placing pipes in which the hot fluid is circulated under the road surface (for HHD) [15] and (ii) locating electric heating cables under the road surface to heat up the road (for EHD) [16]. Both active methods have been applied for a long time in real applications. For instance, while the first application of HHD systems was conducted by the Oregon Highway Department in 1948 using geothermal hot water in Klamath Falls in Oregon, USA, and the project was reconstructed in 1998 [17]; some of the other known projects were (i) the Solar Energy Pilot Project (SERSO) project, which was established on a bridge in Switzerland in 1994 [18], (ii) the Gaia Snow Melting System (Gaia) project, which was applied on road surfaces in Japan in 1996 [19], and (iii) the implemented HHD systems on driveways in Sweden in 2007 [20]. The main purpose of all these projects was to ensure that the road surfaces were kept above 0 °C thanks to the circulated hot fluid in the HHD systems; thereby, the snow and ice formation was prevented on the target road surfaces.

Up until now, many HHD-based efforts to remove snow and ice were done using geothermal heat sources [21–24], but there were also other sources, such as waste heat utilization [25], solar [26–28], and fuels [29]. The first HHD-included studies were mostly based on analytical approaches and then they were followed by basic numerical approaches [30–33]. In the past two decades, more advanced numerical methods were applied via commercial tools [27,34], and they took the surface heat flux, short-wave and long-wave radiation, convection, and conduction into account in comprehensive hydronic snow-melting models validated by experimental data [35–37]. Pahud [38] developed a one-dimensional (1D) numerical model to determine the anti-icing performance of the HHD system applied to the road surfaces of a bridge. In that model, the outside air temperature was used to control the HHD system, and the heating system was activated when the air temperature was between 4 °C and −8 °C. According to the results obtained from the study, it was supposed that the heating system should not be started when the air temperature drops below −8 °C since the risk of ice formation was fairly low due to the low content of air humidity. Abbasi [39] suggested a one-dimensional (1D) numerical model to examine the anti-icing performance of HHD systems applied to road surfaces with two different modes of operation control. The first was to prevent snow and ice formation by keeping the road surface temperature above the freezing point (0 °C). The second control system was considered when the road surface temperature reached below 0 °C, the heating system started to raise the surface temperature above the dew point temperature. It was pointed out that the second control system was much more effective in energy saving. Mirzanamadi et al. [27] carried out simulation studies on the anti-icing performance of the HHD system on roads using the COMSOL Multiphysics 5.2 program. The numerical model, which was verified by experimental data, were performed for many variable parameters that affected the anti-icing performance of the HHD system and those were: pipe spacing, burial depth, the fluid and ambient temperatures, thermal conductivity of the first layer of the road, pipe diameter, emissivity, and absorptivity of the surface. Li and Hong [40] aimed to determine the dynamic heat load of a bridge anti-icing system. The results of the simulation showed that the temperature of the bridge surface was higher than 0 °C, and it was suggested that the theoretically generated heating load and control logic were suitable for bridge anti-icing systems.

Different from the HHD systems, the road surfaces are heated by using electric cables or electric mats to prevent snow and ice formation on the road surfaces in the EHD method [41,42]. The main system components of EHD systems are a heating source (electricity), sensors for measuring the weather conditions (ground sensor and thermostat), a heating element (electric cables or electric mats), and system controllers. In Ref. [43], experimental and numerical studies were carried out on the pavement to determine the

performance of electric snow-melting systems, and computer software was also developed for the transient analysis of electric snow-melting systems in their model validated by the experimental data. Li et al. [44] developed a new heat transfer model to examine the performance of electric snow-melting systems for various road surfaces in different weather conditions. Lai et al. [45] experimentally and numerically investigated the snow-melting process of electric snow-melting systems in a tunnel portal under different conditions. They used the finite element (FE) simulation, and the effects of the insulation layer and ambient temperature on the snow-melting performance were examined in the simulation studies. Liu et al. [46] proposed two methods, a theoretical model and a semi-empirical formula, using the line heat source theory and the virtual image method to determine the temperature field and the road surface temperature of electric snow-melting systems. With the help of those developed methods, the energy consumption characteristics of electric snow-melting systems were investigated [47,48]. Kim et al. [49] studied the energy consumption characteristics of electric snow-melting systems on railroads. The results indicated that the energy consumption was dependent on the system's operating time, and they experimentally observed that the system's operating time increased when the ambient temperature decreased and the wind speed increased.

Besides the above-mentioned application areas of the HHD and EHD methods, they can also be applied to the ramped entry and exit ways of buildings in the winter period, particularly for high-rise buildings in densely populated areas as the car parking is a significant problem in the city and the underground car parks are effective solutions. During the winter period, considering the population and vehicle density, the entry/exit periods for cars not only become time-consuming but also risky due to the snow and ice formation-related slippery conditions. In the present study, we specifically focus on this problem and consider the HHD and EHD methods for a case study in Istanbul city. The HHD model was developed using a numerical heat transfer model with realistic boundary conditions and meteorological data, while the practical applications-based EHD approach was applied for two different EHD cases; (i) applying the EHD to the whole driveway at the entry/exit and (ii) applying the EHD only for tire tracks. The numerical model of the HHD method has the parameters of burial depth (P_d), pipe spacing (P_p), number of parallel pipes (NPP), and the supplied fluid and air temperature to the model. Based on the performance assessment, the most convenient operating conditions are defined with respect to the initial investment cost and the operating cost. Following the given scope, the two main contributions of the current study are (i) to develop a new and numerical time-dependent heat transfer model for the HHD method, and (ii) to perform economic comparisons of HHD and EHD solutions for a specific case study that considers the ramped entry/exit of the underground car parks. Thereby, the obtained outcomes can be used for real-scale applications by construction companies as alternative options to traditional methods.

2. Design of Underground Car Park Roads at the Entry and the Exit

In metropolitan cities, such as Istanbul, the ramped entry and exit ways of underground car parks are high inclination angles; thus, the snow and ice formation on the way makes the safe entry and exit significantly challenging and time-consuming. A representative case is illustrated in Figure 1. The entry and exit areas have a width of 5 m and a length of 8 m. The HHD and EHD solutions are designed for the red-dashed area. In the HHD scenario, cross-linked polyethylene (PEX) pipes are located in the reinforced concrete layer of the driveway. A hot fluid, which is heated by the central heating unit of the building, is circulated through the PEX pipes and prevents snow and ice formation on the road surface. In the EHD scenario, instead of PEX pipes, electric heating cables are placed in the entrance and exit areas of an underground car park with two sub-scenarios; (i) whole driveway and (ii) only tire tracks.

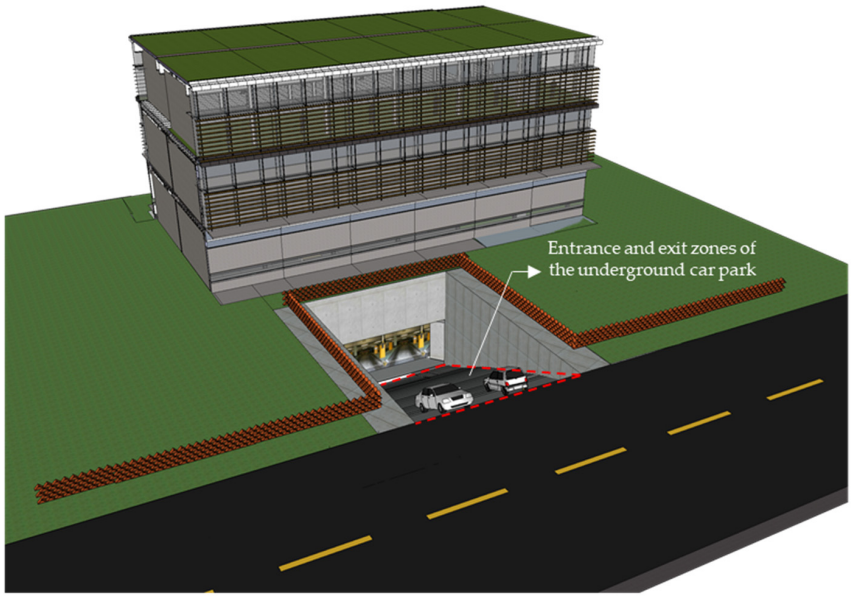

Figure 1. Schematic view of the entrance and exit zone of the underground car park.

2.1. Design of the HHD System

The developed numerical model is a three-dimensional time-dependent heat transfer model with realistic boundary conditions and meteorological data; hereby, the model can obtain the three-dimensional temperature distribution around the PEX pipes placed in the reinforced concrete layer under the underground car park entrance and exit. A simplified projection is given in Figure 2.

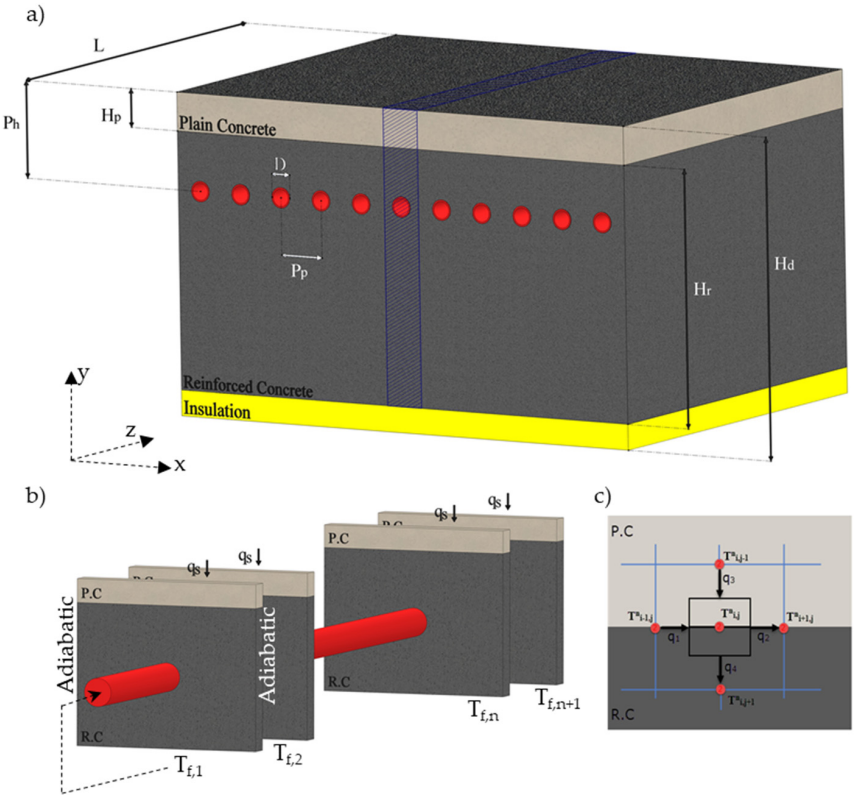

Figure 2. Numerical solution domain of the HHD system; (**a**) the overall isometric view of the domain, (**b**) the solution domain of the model along the z-axis, and (**c**) the energy balance of plain and reinforced concrete interfaces.

The numerical model solves the heat transfer equations in the two-dimensional domain with time-dependent boundary conditions at first; the two-dimensional model also covers the water temperature in the solution domain. The temperature gradient of water along the pipe axis is very small and therefore negligible. After solving Equation (1) in the two-dimensional domain, the solution is extended along the pipe length for obtaining a three-dimensional temperature distribution:

$$\frac{\partial^2 T(x,y,t)}{\partial x^2} + \frac{\partial^2 T(x,y,t)}{\partial y^2} = \frac{1}{\alpha}\frac{\partial T(x,y,t)}{\partial t} \tag{1}$$

where T is temperature; x and y are the coordinates; t is time, and α is the ground diffusivity. We have some assumptions for the model; (i) the horizontal pipes are buried at the same depth in the reinforced concrete environment, (ii) each PEX pipe has the same flow rate without water temperature change in the y-direction, (iii) effects of mass transfer and collectors on the heat transfer are neglected, and (iv) the heat transfer medium (reinforced and plain concrete layers in Figure 2) is assumed homogeneous with the constant thermal properties (conductivity, diffusion, etc.). In Figure 2, the length of the horizontal pipe (L), the pipe spacing (P_p), the vertical distance of the pipe from the road surface (P_h), the vertical length of the plain concrete (H_p), the vertical length of the reinforced concrete (H_r), and the depth of the numerical simulation domain (H_d) are shown; these parameters are actively used in the HHD-based parametric study. The initial and boundary conditions of the numerical model are defined in Equations (2)–(6):

$$T_i = T(y,t) \text{ at } t = 0 \tag{2}$$

$$\left.\frac{\partial T}{\partial x}\right|_{x=P_p/2} = 0 \tag{3}$$

$$\left.\frac{\partial T}{\partial x}\right|_{x=0} = 0 \tag{4}$$

$$\dot{q}\ for\ y = H_d \tag{5}$$

$$\dot{q}_s\ for\ y = 0 \tag{6}$$

where $\dot{q}$ is heat flux, and the subscript s represents the road surface. When the energy balance equation is written for the plain concrete surface, the heat flux of the surface is exerted based on the surface-ambient heat interaction mechanisms and the balance equation can be written as in Equation (7) [50,51]:

$$\dot{q}_s = \dot{q}_c + \dot{q}_m + \dot{q}_{el} + \dot{q}_{il} + \dot{q}_{solar} \tag{7}$$

where $\dot{q}_c$ is the sensible heat flux, $\dot{q}_m$ is the latent heat flux, $\dot{q}_{el}$ is the emitted long-wave radiation-related heat flux, $\dot{q}_{il}$ is the incident long-wave radiation-related heat flux; and $\dot{q}_{solar}$ is the solar radiation heat flux. The $\dot{q}_c$ is defined in Equation (8):

$$\dot{q}_c = \rho_{air} \cdot C_{p,air} \cdot D_h \cdot \xi \cdot (T_{air} - T_s) \tag{8}$$

where ρ is density, C is the specific heat capacity, D_h is the sensible heat exchange coefficient, ξ is the stability function, while the subscript air represents the ambient air. The stability function is explained with the Richardson number (R_i), as shown in Equations (9) and (10),

$$\xi = \frac{1}{(1 + 10\ R_i)} \tag{9}$$

$$R_i = \frac{g \cdot z \cdot (T_{air} - T_s)}{T_{air} \cdot U_z^2} \tag{10}$$

where g is the gravitational acceleration, z is the reference height, and U_z is the wind speed at the height of z. In addition, D_h the term is explained in Equation (11):

$$D_h = \frac{\kappa^2 \cdot U_z}{(ln(z/z_0))^2} \tag{11}$$

where κ is the Von Karman constant, and z_0 is the roughness length. After $\dot{q}_m$, the $\dot{q}_c$ term is given in Equation (12):

$$\dot{q}_m = 0.0168 \cdot f \cdot h_{air} \cdot (P_s - P_{air}) \tag{12}$$

where f is the humidity and surface cover coefficient, h_{air} is the heat transfer coefficient of air, and P is the period (seconds). The $\dot{q}_{el}$ is given in Equation (13):

$$\dot{q}_{el} = -\varepsilon \cdot \sigma \cdot T^4 \tag{13}$$

where ε and σ are the emissivity and the Stefan–Boltzmann coefficient, respectively. The $\dot{q}_{il}$ is given in Equation (14):

$$\dot{q}_{il} = 1.08 \cdot \left(1 - e^{-(0.01\ e_{air})^{T_{air}/2016}}\right) \cdot \sigma \cdot T_{air}^4 \tag{14}$$

where e_{air} is the atmospheric vapor pressure. In the last term, $\dot{q}_{solar}$, is given in Equation (15):

$$\dot{q}_{solar} = (1 - albedo)\left[S_{mean} - S_{amp} \cdot Re \cdot e^{-i\omega t + \varphi_1}\right] \tag{15}$$

where $albedo$ is the reflectivity, S_{mean} is the annual mean solar radiation, S_{amp} is the amplitude of solar radiation, ω is the angular velocity, and φ_1 is the phase angle. In addition to all the heat fluxes on the road surface (sensible heat flux, latent heat flux, emitted and incident long-wave radiation, and solar radiation heat flux) given in Equation (7), the heat conduction and heat flux due to precipitation could have been added in case of snow formation on the road surface. However, in this study, snow formation on the road surface is prevented; therefore, these heat fluxes are not included since there is no additional layer on the road surface.

In order to obtain transient three-dimensional temperature distributions in the entire solution domain, the whole pipe is divided into small sections and the two-dimensional temperature distributions described above are connected to each other. These sections divided along the pipe, starting from the pipe entrance, the fluid temperature leaving from the first section is taken as the fluid inlet temperature of the next section at the same time, and transient three-dimensional temperature profiles are obtained by performing this throughout the pipe (Figure 2). In the line source theory, the surface temperature of the pipe is accepted to be equal to the fluid temperature and solutions are performed accordingly. More details on the theory can be found in Refs. [52,53]. In the developed model, the wall thickness of the pipe is taken into the account and it is assumed that the inner surface temperature of the pipe is equal to the fluid temperature. This approach presents quite reasonable results, especially in cases where the heat transfer coefficient of the fluid flowing in the pipe is high and the pipe diameter is small. Additionally, the horizontal and vertical temperature around the pipe buried in the reinforced concrete, and the fluid inlet and outlet temperatures are determined thanks to the three-dimensional temperature distributions obtained above. Using the energy balance between the pipe and the solution domain in reinforced concrete for each section, the fluid outlet temperatures are calculated as given in Equation (16):

$$T_{f,o} = T_{RC} - \left(T_{RC} - T_{f,i}\right) e^{\frac{-k_{RC} L}{\dot{m}_f C_{p,f}}} \tag{16}$$

where k is the thermal conductivity, whereas the subscripts RC, f, o, and i denote the reinforced concrete, fluid, outlet, and inlet, respectively. The numerical solution domain

is solved by using the alternating direction implicit (ADI) method, which obtains nodal temperatures by applying the difference formulas separately for rows and columns in two successive steps. The finite difference form of Equation (1) in the ADI method is given in Equation (17):

$$\frac{T_{i,j}^{n+1} - T_{i,j}^{n}}{\alpha \Delta t} = \frac{T_{i-1,j}^{n+1} - 2T_{i,j}^{n+1} + T_{i+1,j}^{n+1}}{(\Delta x)^2} + \frac{T_{i,j-1}^{n} - 2T_{i,j}^{n} + T_{i,j+1}^{n}}{(\Delta y)^2} \tag{17}$$

and at $(n+2)^{th}$ time, it can be written in Equation (18):

$$\frac{T_{i,j}^{n+2} - T_{i,j}^{n+1}}{\alpha \Delta t} = \frac{T_{i-1,j}^{n+2} - 2T_{i,j}^{n+2} + T_{i+1,j}^{n+2}}{(\Delta x)^2} + \frac{T_{i,j-1}^{n+1} - 2T_{i,j}^{n+1} + T_{i,j+1}^{n+1}}{(\Delta y)^2} \tag{18}$$

for equal spacing in x- and y-directions, the relation can be defined as given in Equation (19):

$$\Delta x = \Delta y \, , \; \frac{\alpha \Delta t}{(\Delta x)^2} = \frac{\alpha \Delta t}{(\Delta y)^2} = r \tag{19}$$

The unknowns and knowns of each step on the right and left sides of the equations are combined and rewritten as given in Equations (20) and (21):

$$-rT_{i-1,j}^{n+1} + (1+2r)T_{i,j}^{n+1} - rT_{i+1,j}^{n+1} = rT_{i,j-1}^{n} + (1-2r)T_{i,j}^{n} + rT_{i,j+1}^{n} \tag{20}$$

$$-rT_{i,j-1}^{n+2} + (1+2r)T_{i,j}^{n+2} - rT_{i,j+1}^{n+2} = rT_{i-1,j}^{n+1} + (1-2r)T_{i,j}^{n+1} + rT_{i+1,j}^{n+1} \tag{21}$$

In the developed model of the HHD system, two different layers are reinforced concrete and plain concrete. Therefore, the energy balance is exerted for the control volume around each node at the reinforced and plain concrete interface. When the control volume and the heat fluxes around the node are taken into the account (see Figure 2), the energy balance for a node at the layer interface between these concretes is written in Equation (22):

$$\dot{q}_1 - \dot{q}_2 + \dot{q}_3 - \dot{q}_4 = \left(\rho C_p\right)_{ave} (\Delta x)(\Delta y) \frac{\partial T_{i,j}}{\partial t} \tag{22}$$

where $\left(\rho C_p\right)_{ave}$ is the average heat capacity based on the arithmetic mean of the heat capacity values of the reinforced concrete (RC) and the plain concrete (PC) as given in Equation (23):

$$\left(\rho C_p\right)_{ave} = \frac{\left(\rho C_p\right)_{RC} + \left(\rho C_p\right)_{PC}}{2} \tag{23}$$

The heat flux terms of $\dot{q}_1$ and $\dot{q}_2$ are at the interface between the reinforced concrete layer and the plain concrete layer; thus, the thermal conductivity at the interface is defined with the arithmetic mean of the thermal conductivity values of the reinforced concrete and the plain concrete (Equation (24)); then, the $\dot{q}_1$ and $\dot{q}_2$ terms are explained with Equations (25) and (26), respectively:

$$k_{ave} = \frac{k_{RC} + k_{PC}}{2} \tag{24}$$

$$\dot{q}_1 = k_{ave} \frac{T_{i-1,j}^{n} - T_{i,j}^{n}}{\Delta x} \Delta y \tag{25}$$

$$\dot{q}_2 = k_{ave} \frac{T_{i+1,j}^{n} - T_{i,j}^{n}}{\Delta x} \Delta y \tag{26}$$

On the other hand, the heat flux terms of $\dot{q}_3$ and $\dot{q}_4$ are only at the plain concrete layer and the reinforced concrete layer, respectively, and they are defined in Equations (27) and (28), respectively:

$$\dot{q}_3 = k_{PC}\frac{T^n_{i,j-1} - T^n_{i,j}}{\Delta y}\Delta x \tag{27}$$

$$\dot{q}_4 = k_{RC}\frac{T^n_{i,j+1} - T^n_{i,j}}{\Delta y}\Delta x \tag{28}$$

Using the written energy balance for a node at the interface of concrete layers, the difference formulas of the ADI method are reformed to determine new difference formulas at the bottom and top interfacial nodes of the reinforced and plain concrete layers as explained in Equations (29) and (30), respectively,

$$-r_{ave}T^{n+1}_{i-1,j} + (1+2r_{ave})T^{n+1}_{i,j} - r_{ave}T^{n+1}_{i+1,j} = r_{RC}T^{n}_{i,j-1} + (1-r_{RC}-r_{PC})T^{n}_{i,j} + r_{PC}T^{n}_{i,j+1} \tag{29}$$

$$-r_{RC}T^{n+2}_{i,j-1} + (1+r_{RC}+r_{RC})T^{n+2}_{i,j} - r_{PC}T^{n+2}_{i,j+1} = r_{ave}T^{n+1}_{i-1,j} + (1-2r_{ave})T^{n+1}_{i,j} + r_{ave}T^{n+1}_{i+1,j} \tag{30}$$

The temperature distribution in reinforced and plain concrete at a certain time is solved successively using the ADI formulation equations. Since the resulting matrices have tri-diagonals, these equations are solved using the Thomas algorithm. Consequently, all the ADI finite difference equations of the HHD system are solved by integrating them into the MATLAB program with realistic boundary conditions and meteorological data.

2.2. Design of the EHD System

The EHD system works by radiating heat upward from a grid of heating cables under the driveway surface, preventing the formation of snow and ice. Two sub-application methods of the EHD solution, the whole driveway and the only tire tracks, were considered. In both application methods, the electric heating cables are placed in the concrete layer with a burial depth of 6 cm. Below the plain concrete layer, there are two more concrete layers; the foam concrete (used for an insulation layer) and the reinforced concrete [46,54], as shown in Figure 3a.

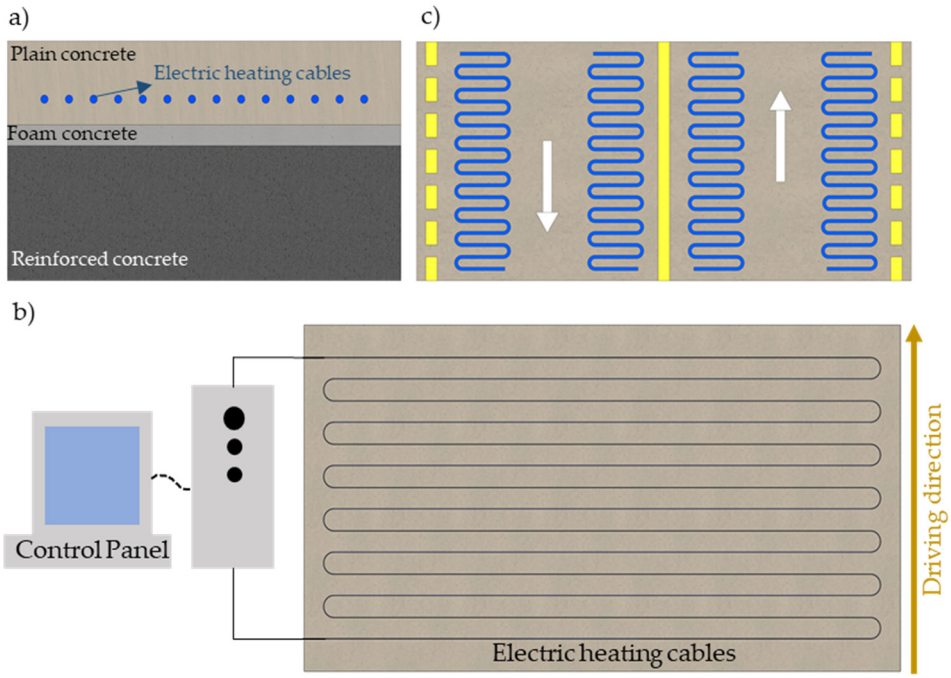

Figure 3. A simplified view of the EHD system; (**a**) schematic, (**b**) whole driveway case, and (**c**) only tire track case.

In the first scenario, the electric cables are placed on the whole driveways with (i) two electric heating cables with a length of 215 m and a heating power rate of 5840 W and (ii) a single cable with a length of 110 m and a heat power rate of 2910 W, which nearly corresponds to the heating power rate of 27 W per unit of the cable length, which is also in good agreement with commercial references [55] and recent calculations in the literature [56]. As can be seen in Figure 3b, 108 rows of electric heating cables are used at a distance of 74 mm from one another. In the second scenario, the same heating power rate per unit of the cable length is aimed (27 W). Only for tire tracks (Figure 3c), two electric cables with a length of 140 m, and a heating power rate of 3780 W are used. Following the tire tracks, the electric cables are spaced 23 mm apart on each of the four parallel electrical heating cables by using 350 rows.

3. Economic Model

3.1. Economic Model of the HHD Method

The HHD systems have the main costs of the initial investments as follows; pipe cost (C_{pipe}), heat exchanger costs (C_{HX}), pumping costs (C_{pump}), cost of the control system ($C_{control}$), costs of the thermostat and ground sensor (C_{sensor}), labor costs (C_{labor}), and auxiliary costs (C_{aux}). Among them, the costs of the heat exchanger and pipe (with connection/fitting equipment) have the biggest shares. Besides the investment cost terms, operating costs are also critical. In the current HHD scenario, the central heating system of the building is aimed to be used to provide hot fluid; thus, the cost of the supplied heat from the central heating system is indexed to the natural gas prices while the pumping power-related cost is indexed to the electricity price in Istanbul. Using the collected performance output from the developed numerical model, the total cost analysis is performed by using the ten-year average escalation rates. The cost of initial investment (C_i) is defined in Equation (31):

$$C_i = C_{pipe} + C_{HX} + C_{control} + C_{sensor} + C_{pump} + C_{aux} + C_{labor} \quad (31)$$

For the pipe, heat exchanger, and pump, cost functions are used and they are defined in Equations (32)–(34), respectively.

$$C_{pipe} = c_{pipe} \cdot N \cdot L \quad (32)$$

$$C_{HX} = a_1 \dot{Q}_{HX}^{a_2} \quad (33)$$

$$C_{pump} = a_3 \dot{W}_{pump}^{a_4} \quad (34)$$

where c_{pipe} is the unit cost of the pipe (per meter), N is the number of pipes, L is the length of each pipe, Q_{HX} is the heat transfer rate through the heat exchanger, W_{pump} is the required power rate for pumping operation, and the coefficients $a_1 - a_4$ are determined by the different load requirements of the HHD system and the regional price of the equipment. For the operating costs, the total electric consumption of the HHD system is directly related to the pump operation and the electric consumption of the pump (E_{pump}) is explained in Equation (35):

$$E_{pump} = \tau \frac{V_f \cdot dP_{pump}}{\eta_{pump}} \quad (35)$$

where V is the volumetric flow rate, τ is the total operating hours, dP is the differential pressure across the flow path, and η_{pump} is the pump efficiency. Then, the cost of total electricity consumption ($C_{electricity}$) is calculated by using Equation (36):

$$C_{electricity} = E_{pump} \cdot c_{tariff} \quad (36)$$

where c_{tariff} is the tariff of the unit electricity consumption (for residential purposes) obtained from the Energy Market Regulatory Authority (EMRA) of Turkey. The cost of

natural gas consumption (referring to the use of the central heating unit of the building to provide a hot fluid stream), is calculated by using the required heat rate of the ground heat exchanger (Equation (37)), and the unit cost of natural gas (c_{NG}) as given in Equation (38):

$$\dot{Q}_{HX} = \tau \cdot \rho \cdot V_f \cdot C_p \cdot \left(T_{f,i} - T_{f,o} \right) \tag{37}$$

$$C_{NG} = \dot{Q}_{HX} \cdot c_{NG} \tag{38}$$

The unit cost of gas (c_{NG}) is received from the Petroleum Pipeline Corporation of Turkey (BOTAS). The ten-year average escalation rates of natural gas and electricity for residences in Turkey are 10% and 15%, respectively. The total consumption costs of electricity and natural gas (C_{op}) in ten years are obtained using Equation (39) [57]:

$$C_{op} = \left(C_{electricity,1} + \sum_{n=2}^{n=10} C_{electricity,n} \cdot e \right) + \left(C_{NG,1} + \sum_{n=2}^{n=10} C_{NG,n} \cdot g \right) \tag{39}$$

where the subscripts e and g are defined as the increase rate of electricity and natural gas prices, respectively. The C_{op} refers to the operating costs. The summation of the operating costs and the investment cost is multiplied by the capital recovery factor, CRF, (Equation (40)) to calculate the cumulative cost as defined in Equation (41):

$$CRF = \frac{i(i+1)^n}{(i+1)^n - 1} \tag{40}$$

$$C_{tot} = \left(C_{op} + C_i \right) \cdot CRF \tag{41}$$

3.2. Economic Model of the EHD Method

The EHD method needs less heating time with low-priced installation and maintenance costs compared to the HHD; however, the operating costs can be higher than the HHD due to higher electricity prices than the natural gas price. Regarding the aimed application methods of the EHD with (i) whole driveways and (ii) only tire tracks. The tire-track-based EHD is preferable for individual or domestic usage since it needs fewer operating costs, while the whole driveways-based EHD is more secure and therefore preferable in crucial public and transportation areas, such as hospitals and airports. The investment costs of the EHD method are as follows; cable cost (C_{cable}), cost of the control system ($C_{control}$), costs of the thermostat and ground sensor (C_{sensor}), labor costs (C_{labor}), and auxiliary costs (C_{aux}). For the whole driveways and the tire-track solutions, the only difference is the cable cost. Considering all terms, the investment cost (C_i) can be defined in Equation (42) [58]:

$$C_i = C_{cable} + C_{control} + C_{sensor} + C_{aux} + C_{labor} \tag{42}$$

The cost of the electric heating cable is defined by using the unit cost (c_{cable}) and the length of the cable as given in Equation (43):

$$C_{cable} = c_{cable} \cdot L_{cable} \tag{43}$$

The operating costs of the EHD method only depend on the electricity prices; thus, the total electricity consumption is found first (Equation (44)); then, the electricity price is calculated by using Equation (45):

$$E_{cable} = \tau \cdot \beta_{cable} \cdot L_{cable} \tag{44}$$

$$C_{electricity} = E_{cable} \cdot c_{tariff} \tag{45}$$

where β_{cable} is the power drawn per meter by the EHD system. The operating costs over ten years are calculated using Equation (46); then, the cumulative cost can be found with Equation (41):

$$C_{op} = \left(C_{electricity,1} + \sum_{n=2}^{n=10} C_{electricity,n} \cdot e \right) \quad (46)$$

4. Simulations

Based on the developed numerical model of the HHD system, the key inputs of the numerical model are given in Table 1 while the all details of parametric conditions are explained in Table 2. The HHD simulations are organized as eight sets according to the model parameters of burial depth (P_d), pipe spacing (P_p), number of parallel pipes (NPP), and the supplied fluid and air temperature to the model.

Table 1. HHD system inputs in the simulation.

Layers and Components	Input Values
Working fluid (Water + Ethylene Glycol)	V_f = 1.143 m^3/h
Plain concrete	k_{PC} = 0.7 W/mK, C_P = 920 J/kgK, ρ = 2110 kg/m^3
Reinforced concrete	K_{RC} = 2.5 W/mK, C_P = 750 J/kgK, ρ = 2400 kg/m^3
Concrete layers height	H_c = 0.36 m, H_p = 0.06 m
Pipe (PEX)	k_p = 0.40 W/mK
Pipe geometry	L = 8 m D_o/D_i = 0.015/0.010 m

Table 2. Parametric sets of the HHD system.

	Parameters	Parameter level	Units
Set 1	Burial depth (P_d)	0.1, 0.15, 0.20, 0.25	m
	Pipe spacing (P_p)	0.1	m
	Number of parallel pipes (NPP)	50	-
	Supplied fluid temperature ($T_{f,in}$)	10	°C
	Air temperature (T_{air})	0	°C
Set 2	Supplied fluid temperature ($T_{f,in}$)	10, 20, 30, 40	°C
	Pipe spacing (P_p)	0.1	m
	Number of parallel pipes (NPP)	50	-
	Burial depth (P_d)	0.1	m
	Air temperature (T_{air})	0	°C
Set 3	Supplied fluid temperature ($T_{f,in}$)	10, 20, 30, 40	°C
	Air temperature (T_{air})	−5	°C
	Number of parallel pipes (NPP)	50	-
	Burial depth (P_d)	0.1	m
	Pipe spacing (P_p)	0.1	m
Set 4	Supplied fluid temperature ($T_{f,in}$)	10, 20, 30, 40,50	°C
	Air temperature (T_{air})	−10	°C
	Number of parallel pipes (NPP)	50	-
	Burial depth (P_d)	0.1	m
	Pipe spacing (P_p)	0.1	m
Set 5	Supplied fluid temperature ($T_{f,in}$)	10, 20, 30	°C
	Air temperature (T_{air})	−5	°C
	Number of parallel pipes (NPP)	100	-
	Burial depth (P_d)	0.1	m
	Pipe spacing (P_p)	0.05	m

Table 2. *Cont.*

	Parameters	Parameter level	Units
Set 6	Supplied fluid temperature ($T_{f,in}$)	10, 20, 30, 40	°C
	Air temperature (T_{air})	−10	°C
	Number of parallel pipes (NPP)	100	-
	Burial depth (P_d)	0.05	m
	Pipe spacing (P_p)	0.1	m
Set 7	Supplied fluid temperature ($T_{f,in}$)	30, 40, 50, 60	°C
	Air temperature (T_{air})	−5	°C
	Number of parallel pipes (NPP)	25	-
	Burial depth (P_d)	0.1	m
	Pipe spacing (P_p)	0.2	m
Set 8	Supplied fluid temperature ($T_{f,in}$)	30, 40, 50, 60, 70	°C
	Air temperature (T_{air})	−10	°C
	Number of parallel pipes (NPP)	25	-
	Burial depth (P_d)	0.1	m
	Pipe spacing (P_p)	0.2	m

Similar to the HHD system, the key input values of the EHD system are listed in Table 3 based on Refs. [51,53]. In Table 3, D_{cable}, L_{cable}, HP_{cable}, and N_{cable} represent embedded depth, length, heating power, and the number of electric heating cables, respectively. In addition, B_{cable} is the distance between the electric heating cables.

Table 3. EHD system inputs in the comparative study.

Type of EHD System	Input Value
Whole driveways	D_{cable} = 0.06 m B_{cable} = 0.074 m HP_{cable} = 14,590 W L_{cable} = 540 m N_{cable} = 108
Only tire tracks	D_{cable} = 0.06 m B_{cable} = 0.023 m HP_{cable} = 7560 W L_{cable} = 280 m N_{cable} = 350

Besides the system input values and the parametric sets, the numerical values of the economic parameters of the HHD and EHD systems are given in Tables 4 and 5, respectively.

Table 4. Economic parameters of the HHD system.

Case	Cost Parameter	Description
Common costs for all NPP cases	Pipe	C_{pipe} = 1.66 (€/m)
	Energy-control group	$C_{control}$ = 400 (€)
	Ground sensor and thermostat	C_{sensor} = 500 (€)
	Heat exchanger	C_{HX} = 1000 (€)
	Tariff on unit electricity consumption	c_{tariff} = 0.12 (€/kWh)
	Price per unit kWh of natural gas	c_{NG} = 0.021 (€/kWh)
	Increase rate of electricity price	e = 10%, 15%, 20%
	Increase rate of natural gas price	g = 5%, 10%, 15%
	Interest rate	i = 12%
	Number of interest periods	n = 10 year
	Working time of the pump	τ = 120 h
	Pump efficiency	η_{pump} = 80%

Table 4. *Cont.*

Case	Cost Parameter	Description
$NPP = 25$	Circulation pump	C_{pump} = 53 (€)
	Additional (materials and pipework)	C_{aux} = 555 (€)
	Total labor	C_{labor} = 655 (€)
$NPP = 50$	Circulation pump	C_{pump} = 66 (€)
	Additional (materials and pipework)	C_{aux} = 944 (€)
	Total labor	C_{labor} = 770 (€)
$NPP = 100$	Circulation pump	C_{pump} = 95 (€)
	Additional (materials and pipework)	C_{aux} = 1666 (€)
	Total labor	C_{labor} = 998 (€)

Table 5. Economic parameters of the EHD system.

Case	Cost Parameter	Description
Common costs for all *NPP* cases	Heating cables	C_{cable} = 1.66 (€/m)
	Energy-control group	$C_{control}$ = 400 (€)
	Ground sensor and thermostat	C_{sensor} = 500 (€)
	Power drawn per unit meter	h_c = 27 (W/m)
	Increase rate of electricity price	e = 10%, 15%, 20%
	Interest rate	i = 12%
	Number of interest periods	n = 10 year
	Tariff on unit electricity consumption	c_{tariff} = 0.12 (€/kWh)
Whole driveways	Additional	C_{aux} = 200 (€)
	Total labor	C_{labor} = 880 (€)
Only tire tracks	Additional	C_{aux} = 80 (€)
	Total labor	C_{labor} = 550 (€)

5. Results and Discussion

The developed numerical heat transfer model was validated by using the experimental dataset given by Demir et al. [59] for a ground heat exchanger model. Figure 4 compares the time-dependent temperature values between the current numerical model and the given experimental dataset based on the hydronic heating approach.

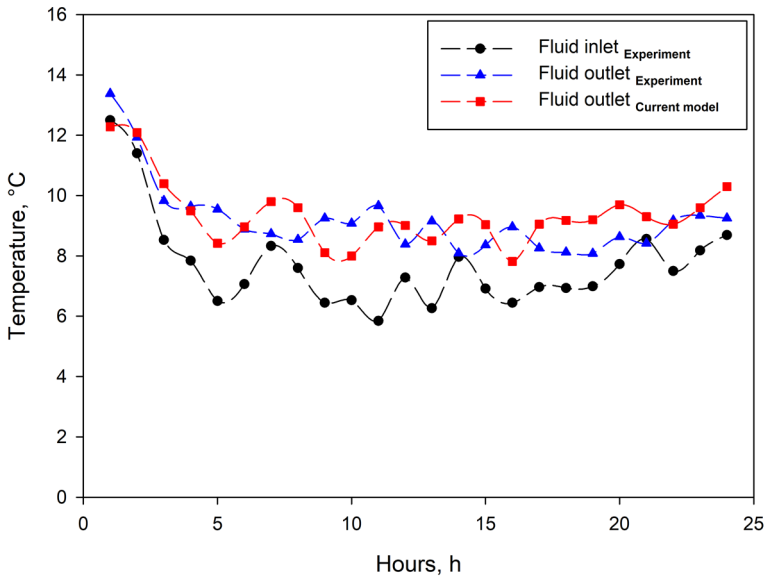

Figure 4. Validation of the developed numerical model with an experimental dataset by Demir et al. [59].

The HHD system is analyzed at different parametric simulations; the main parameters are the burial depth, supplied fluid temperature, air temperature, and pipe spacing. Figure 5a shows the temperature distribution in vertical distance from the road surface according to different burial depths at $T_{f,in}$ = 10 °C, P_p = 0.1 m (NPP = 50) and T_{air} = 0 °C. The vertical temperature distribution from H_d = 0 (road surface) to the simulation depth is given in Figure 5a, by taking the different burial depths (P_d) of 0.1 m, 0.15 m, 0.2 m, and 0.25 m into account. Icing starts at 0 °C on the road surface, and the beginning of the icing problem occurs at burial depths greater than P_d = 0.2 m. The highest temperature is obtained at P_d = 0.1 m, where the burial depth is the closest to the surface. It is seen that PEX pipes being close to the road surface is an important result in preventing the formation of snow and ice. In addition, because the fluid is supplied through the pipe at $T_{f,in}$ = 10 °C at the depth where the pipe is buried, the highest temperature occurs in this area at all burial depths, while the temperature does not change much towards deeper depths. In Figure 5b, the impact of various supplied fluid temperatures is investigated with the values of 10 °C, 20 °C, 30 °C, and 40 °C, while T_{air} = 0 °C and P_p and P_d values are 0.1 m. There is no snow and ice formation on the road surface even for the lowest fluid temperature, and inherently the temperature of the road surface reaches the highest at 40 °C. Considering this parametric set in our case study, it can be said that the supplied fluid temperature of 10 °C is sufficient to prevent snow and ice formation when P_p, P_d, and T_{air} are 0.1 m, 0.1 m, and 0 °C, respectively.

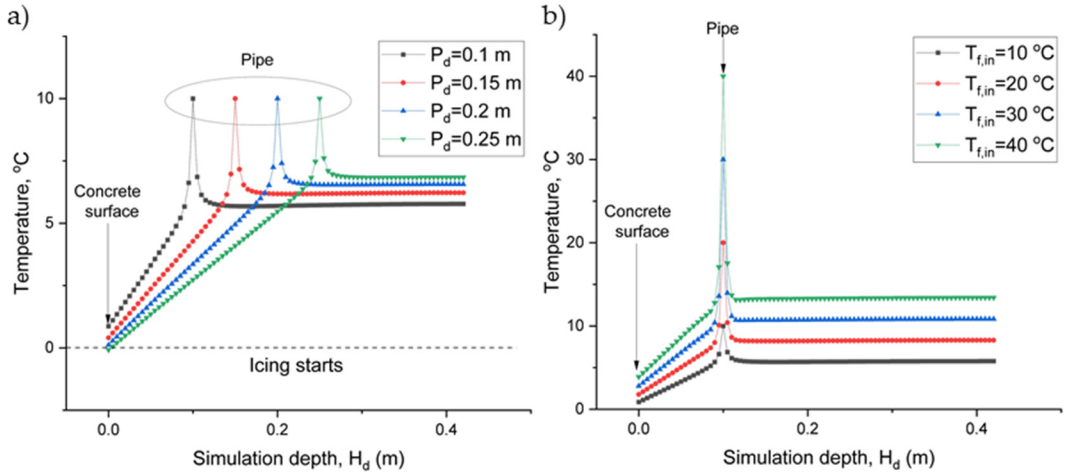

Figure 5. Vertical temperature distribution of (**a**) different supplied fluid temperatures and (**b**) different burial depths at the air temperature of 0 °C.

When the air temperature drops from 0 °C to −5 °C and −10 °C, respectively, the vertical temperature distribution of the HHD system is plotted in Figure 6a,b, respectively, while the P_p and P_d values are 0.1 m. For the air temperature of −5 °C (Figure 6a), it is seen that the supplied fluid temperature values below 35 °C cannot prevent snow and ice formation on the road surface, but higher temperatures are able to keep the road surface temperature above 0 °C. At the air temperature of −10 °C (Figure 6b), only the supplied fluid temperature of 50 °C is capable of preventing snow and ice formation on the road surface. Considering the practical applicability of the presented HHD system, high-supplied fluid temperatures can result in energy losses; thus, the current case (P_p and P_d values are 0.1 m) does not seem sufficient for snow and ice melting on the road surface at air temperatures below 0 °C.

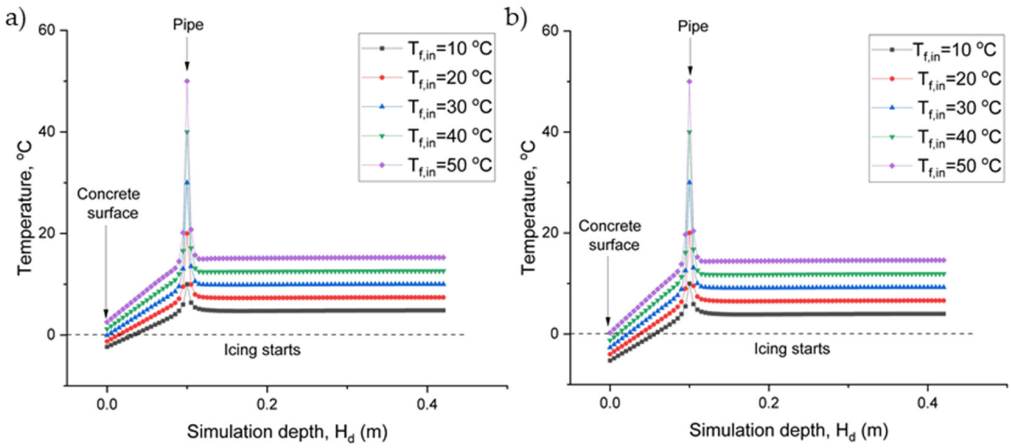

Figure 6. Vertical temperature distribution of PEX pipes at the air temperature of (**a**) −5 °C and (**b**) −10 °C for P_p= 0.1 m.

To prevent the formation of snow and ice at extreme winter conditions, pipe spacing is decreased from 0.1 m to 0.05 m and the numerical model is operated for the same air temperatures of −5 °C and −10 °C, as projected in Figure 7a,b, respectively. When P_p is changed from 0.1 m to 0.05 m, it is seen that the minimum applicable supplied fluid temperature value drops from 35 °C to below 25 °C at the air temperature of −5 °C (Figure 7a). Similarly, at the air temperature of −10 °C (Figure 7b), the required supplied fluid temperature decreases to 40 °C. The supplied fluid temperature range of 20 °C–40 °C is usually an operable range for low-temperature heating solutions in residential applications; therefore, the proposed HHD system can be combined with low-temperature heating solutions in near future works.

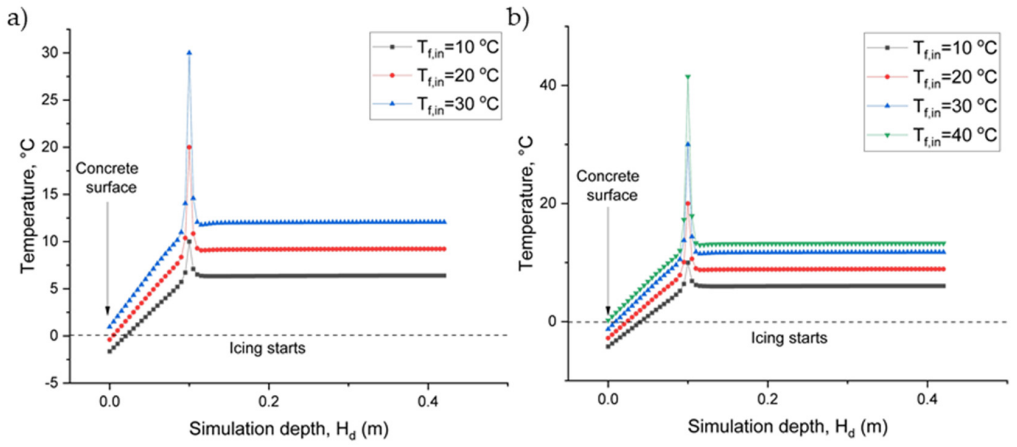

Figure 7. Vertical temperature distribution of PEX pipes at the air temperature of (**a**) −5 °C and (**b**) −10 °C for P_p = 0.05 m.

In case of the availability of high-temperature heat sources, such as boilers, etc. in the target building, higher supplied fluid temperatures can be considered even if they may result in higher energy losses. Thus, we increase the pipe spacing and supply the fluid temperature with higher temperature values. Figure 8a,b show the vertical temperature distribution of PEX piping with P_p = 0.2 m at the air temperatures of −5 °C and −10 °C, respectively. It is seen that the supplied fluid temperature of 50 °C and 70 °C are applicable for Figure 8a,b, respectively. By being able to apply high supply fluid temperatures, we can decrease the required pipe amount. Thus, the increase in fluid temperature may result in an increment in operating costs but also drops in the pipe investment cost.

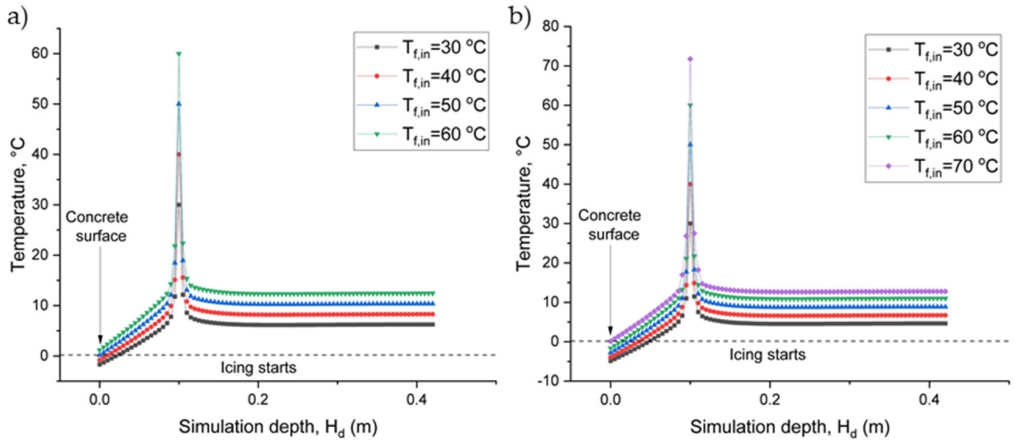

Figure 8. Vertical temperature distribution of PEX pipes at the air temperature of (**a**) −5 °C and (**b**) −10 °C for P_p = 0.2 m.

Considering the extreme weather conditions (the air temperatures of −5 °C and −10 °C), we can decide the most convenient operation conditions with respect to the pipe spacing and supplied fluid temperature by keeping the burial depth constant at 0.1 m. For pipe spacings of 0.05 m, 0.1 m, and 0.2 m, the corresponding number of parallel pipes (NPP) becomes 100, 50, and 25, respectively. Based on these three different NPP values, the minimum applicable supplied fluid inlet temperatures are found by using the numerical heat transfer model, and the vertical temperature distributions are presented for all these cases in Figure 9. At an air temperature of −5 °C (Figure 9a), it is deduced that the minimum supplied fluid temperature is 30 °C for NPP = 100, and it is followed by 40 °C for NPP = 50, and lastly 50 °C for NPP = 25. At the air temperature of −10 °C (Figure 9b), the minimum applicable fluid temperature is 40 °C for NPP = 100, while the maximum is 70 °C for NPP = 25. The selection of the most convenient case depends on the investment and operating costs.

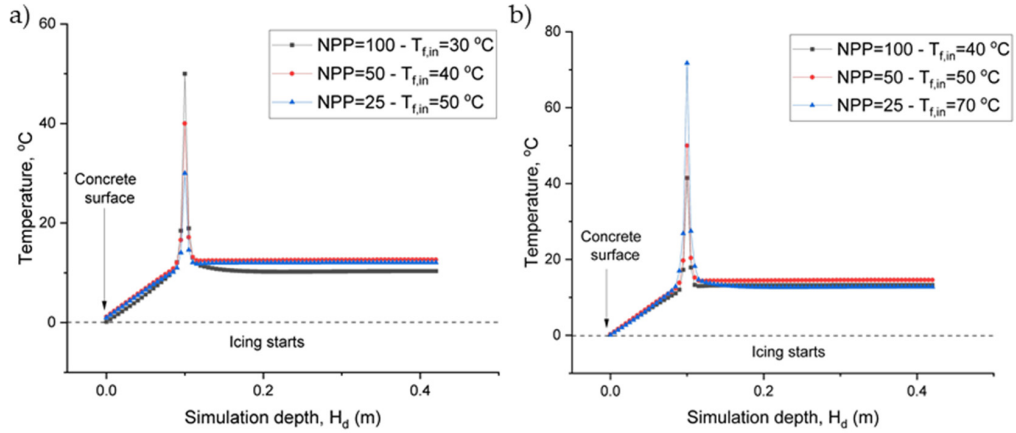

Figure 9. Vertical temperature distribution of PEX pipes at the most convenient cases for the air temperatures of (**a**) −5 °C and (**b**) −10 °C.

Following the thermal performance of the HHD system based on the numerical heat transfer model, Figure 10 presents the economic performance analysis of the HHD system according to the parametric values of pipe spacing (and therefore the NPP), air temperature, the (ten years) increase in natural gas price, and the (ten years) increase in electricity price. In addition, using the increase in electricity price, the economic performance of the EHD system (for both the whole driveway and only tire tracks cases) is analyzed. At the highest air temperature value (0 °C), when the g and e terms are 15% and 20%, respectively, the total HHD cost is calculated as EUR 4120, 3805, and 4780 for the NPP of 25, 50, and 100,

respectively. Using the same g and e values, the NPP of 25, 50, and 100 have the total HHD cost of EUR 4964, 4855, and 5415, respectively, at an air temperature of −5 °C, while the total HHD cost goes up to EUR 5807, 5280, and 5840 for the NPP of 25, 50, and 100 at an air temperature of −10 °C. The economic comparison denotes that the piping case with NPP = 50 is the best trade-off scenario when both investment and operating costs are taken into account. It is also seen that the decrease in air temperature results in increments in the total cost term; the greatest increment belongs to the NPP of 25, while the smallest increment is calculated for the NPP of 100. This shows that a potential application of the HHD system must be critically analyzed from the standpoint of the investment cost term. Figure 10 also plots the economic performance of the EHD system according to the (ten-year) increase in electricity prices. For all e cases, the whole driveway scenario has a higher total cost than the only tire tracks scenario since both investment and operating costs are higher in the whole driveway scenario. At the e of 10%, 15%, and 20%, the total EHD cost is as high as 1.70, 1.72, and 1.74 times for the whole driveway scenario, which shows that the impact of the operating costs is slightly more dominant than the investment cost even though both the investment and operating cost significantly affect the total EHD cost. Based on the given discussions for Figures 5–10, it is worth noting that the volumetric flow rate has also a critical effect which can remarkably affect the hydronic heating performance and therefore the ice formation. The increase in the flow rate provides better heating performance while resulting in a higher operating cost at the constant fluid inlet temperature. That is, the design of operating conditions needs a trade-off analysis regarding the thermal and economic trends.

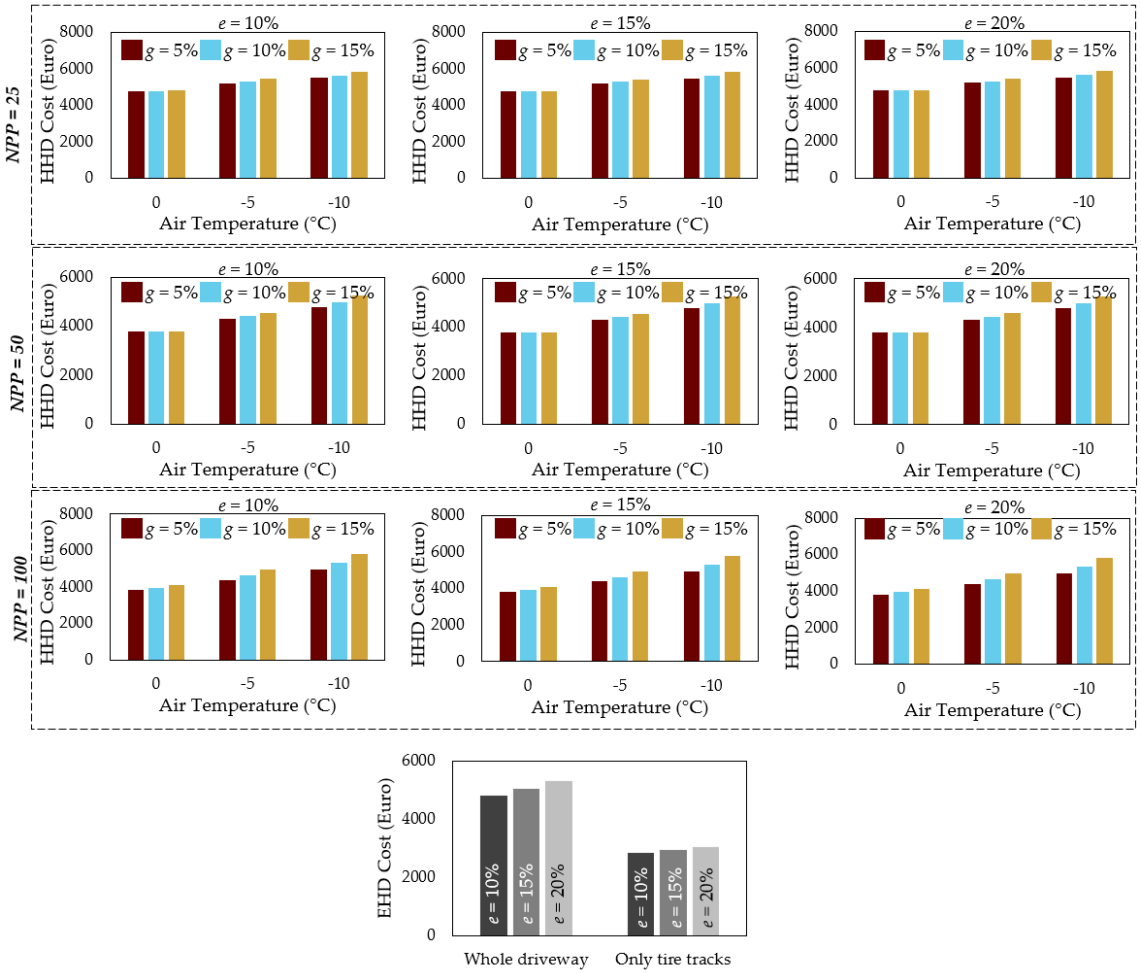

Figure 10. The total cost of the HHD and EHD systems for different NPP, g and e values.

After carrying out individual economic analysis for both the HHD and EHD systems, Figure 11 shows a comparative analysis for three different values of the e term while the g term is constant at 15%, and the NPP case of 50 is selected since it is found the most convenient case among others. The EHD-only tire tracks scenario is the most affordable one in all conditions thanks to its remarkably lower investment and operating costs. It is therefore the most preferable and economic solution except for critical locations and applications, such as hospitals, airports, public administration buildings, etc. Even the g = 5% cases (Figure 10) are considered in the comparison. The HHD system has always a higher total cost than the EHD-only tire tracks scenario. However, when the HHD is compared to the EHD-whole driveways scenario, it is definitely a more feasible method at the air temperature values of 0 °C and −5 °C. At the air temperature of −10 °C, the HHD system is still more feasible when the e = 20%, but the EHD-whole driveway system is better at the e of 10% and 15%.

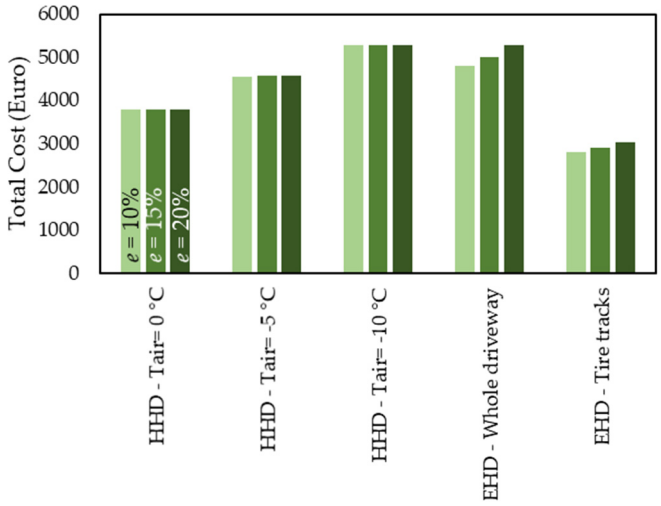

Figure 11. Comparison of total costs for the HHD and EHD cases.

To this end, in case of a continuous and secure electricity supply, the EHD-only tire tracks can be the first option. However, when the electricity supply and security are risky, the HHD system should be chosen (in case of accessibility to hot water sources). Alternatively, as one of the future research points, the possibility of HHD-only tire tracks can be developed and investigated with the numerical approach.

6. Conclusions

The presented study developed a numerical heat transfer model for hydronic heating applications in anti-icing solutions. The model was a three-dimensional and transient model with thermal boundary conditions of the meteorological database. Based on the developed numerical model, an HHD case study was created according to the parameters of ambient air temperature, pipe spacing, burial depth, and supplied fluid temperature for a target building in Istanbul. After that, the economic model was built and the comparison was performed with the EHD applications of (i) the whole driveway scenario and (ii) only the tire tracks scenario. The main conclusions are as follows:

- A better anti-icing solution was observed when the PEX pipes were located closer to the road surface; however, the closest distance should be determined by considering the safety of the HHD setup in winter operations.
- Among three different pipe spacing scenarios, the NPP case of 50 was found as the most convenient solution as it provided the best trade-off economic performance for preventing snow and ice formation on the road surface.

- The decrease of NPP provided a significant decrement in the investment cost, but higher supplied fluid temperatures (and therefore the operating costs) were required to prevent snow and ice formation.
- Both the investment and operating costs were significant for the total costs of the EHD cases; however, the operating cost was slightly more dominant than the investment costs.
- The EHD-only tire track scenario remarkably decreased the total cost, and therefore it was the most economic way when affordability was the main decision objective.
- Compared to the EHD whole driveway scenario and the HHD cases, the HHD was found more feasible for all g and e values at the ambient air temperature of 0 °C and −5 °C, while it was more feasible only for e = 20% at the ambient air temperature of −10 °C.

In light of the foregoing, the developed numerical model states that the HHD is an economically competitive way of anti-icing solutions and better improvements can be performed or developed, such as re-designing the HHD scheme with the only tire tracks option, similar to the EHD-only tire track scenario. Future works can also focus on a broader investigation that considers other parameters (e.g., flow rate) and climatic regions with longer-day requirements for anti-icing and more extreme weather conditions.

Author Contributions: Conceptualization, N.K. and B.B.K.; methodology, N.K.; software, N.K.; validation, N.K. and B.B.K.; formal analysis, N.K.; investigation, N.K.; resources, N.K.; data curation, N.K. and B.B.K.; writing—original draft preparation, N.K. and B.B.K.; writing—review and editing, N.K. and B.B.K.; visualization, N.K. and B.B.K.; supervision, N.K. and B.B.K.; project administration, N.K. and B.B.K.; funding acquisition N.K. and B.B.K. All authors have read and agreed to the published version of the manuscript.

Funding: This research received no external funding.

Institutional Review Board Statement: Not applicable.

Informed Consent Statement: Not applicable.

Data Availability Statement: Not applicable.

Acknowledgments: The authors would like to thank the support from their universities.

Conflicts of Interest: The authors declare no conflict of interest.

References

1. Andreescu, M.P.; Frost, D.B. Weather and Traffic Accidents in Montreal, Canada. *Clim. Res.* **1998**, *9*, 225–230. [CrossRef]
2. Norrman, J.; Eriksson, M.; Lindqvist, S. Relationships between Road Slipperiness, Traffic Accident Risk and Winter Road Maintenance Activity. *Clim. Res.* **2000**, *15*, 185–193. [CrossRef]
3. Call, D.A.; Flynt, G.A. The Impact of Snowfall on Crashes, Traffic Volume, and Revenue on the New York State Thruway. *Weather Clim. Soc.* **2022**, *14*, 131–141. [CrossRef]
4. Li, H.; Xi, W.; Zhang, L.; Zang, S. Snow-Disaster Risk Zoning and Assessment in Heilongjiang Province. *Sustainability* **2021**, *13*, 14010. [CrossRef]
5. Wang, H.; Jasim, A.; Chen, X. Energy Harvesting Technologies in Roadway and Bridge for Different Applications–A Comprehensive Review. *Appl. Energy* **2018**, *212*, 1083–1094. [CrossRef]
6. Gholikhani, M.; Roshani, H.; Dessouky, S.; Papagiannakis, A.T. A Critical Review of Roadway Energy Harvesting Technologies. *Appl. Energy* **2020**, *261*, 114388. [CrossRef]
7. Ghalandari, T.; Hasheminejad, N.; Van den bergh, W.; Vuye, C. A Critical Review on Large-Scale Research Prototypes and Actual Projects of Hydronic Asphalt Pavement Systems. *Renew. Energy* **2021**, *177*, 1421–1437. [CrossRef]
8. Li, S.; Shen, Y.; Dong, J.; Ma, W.; Lv, Y.; Ren, S.; Xie, J.; Ji, S.; Xu, J.; Wang, X. Freezing Damage to Tunnels in Cold Regions and Weights of Influencing Factors. *Sustainability* **2022**, *14*, 14637. [CrossRef]
9. O'hern, S.; Utriainen, R.; Tiikkaja, H.; Pöllänen, M.; Sihvola, N. Exploratory Analysis of Pedestrian Road Trauma in Finland. *Sustainability* **2021**, *13*, 6715. [CrossRef]
10. Yu, W.; Yi, X.; Guo, M.; Chen, L. State of the Art and Practice of Pavement Anti-Icing and de-Icing Techniques. *Sci. Cold Arid. Reg.* **2014**, *6*, 14–21. [CrossRef]
11. Reinosdotter, K.; Viklander, M. Road Salt Influence on Pollutant Releases from Melting Urban Snow. *Water Qual. Res. J. Can.* **2007**, *42*, 153–161. [CrossRef]

12. Sassani, A.; Arabzadeh, A.; Ceylan, H.; Kim, S.; Sadati, S.M.S.; Gopalakrishnan, K.; Taylor, P.C.; Abdualla, H. Carbon Fiber-Based Electrically Conductive Concrete for Salt-Free Deicing of Pavements. *J. Clean. Prod.* **2018**, *203*, 799–809. [CrossRef]
13. Shi, X.; Jungwirth, S.; Akin, M.; Wright, R.; Fay, L.; Veneziano, D.A.; Zhang, Y.; Gong, J.; Ye, Z. Evaluating Snow and Ice Control Chemicals for Environmentally Sustainable Highway Maintenance Operations. *J. Transp. Eng.* **2014**, *140*, 05014005. [CrossRef]
14. Rasul, A.; Seo, J.; Xu, S.; Kwon, T.J.; MacLean, J.; Brown, C. Optimization of Snowplow Routes for Real-World Conditions. *Sustainability* **2022**, *14*, 13130. [CrossRef]
15. Cui, Y.; Zhang, F.; Shao, Y.; Twaha, S.; Tong, H. Techno-Economic Comprehensive Review of State-of-the-Art Geothermal and Solar Roadway Energy Systems. *Sustainability* **2022**, *14*, 10974. [CrossRef]
16. Mensah, K.; Choi, J.M. Review of Technologies for Snow Melting Systems. *J. Mech. Sci. Technol.* **2015**, *29*, 5507–5521. [CrossRef]
17. Lund, J.W. Reconstruction of a Pavement Geothermal Deicing System. *Geo-Heat Cent. Q. Bull.* **1999**, *20*, 14–17.
18. Eugster, W.J.; Schatzmann, J. Harnessing Solar Energy for Winter Road Clearing on Heavily Loaded Expressways. In Proceedings of the XIth PIARC International Winter Road Congress, Sapporo, Japan, 28–31 January 2002; p. 9.
19. Morita, K.; Tago, M. Operational Characteristics of the GAIA Snow-Melting System in Ninohe, Iwate, Japan. *Geo-Heat Cent. Bull.* **2000**, *21*, 5–11.
20. Eugster, W.J. Road and Bridge Heating Using Geothermal Energy, Overview and Examples. In Proceedings of the European Geothermal Congress, Unterhaching, Germany, 30 May–1 June 2007; p. 5.
21. Baumgärtel, S.; Schweighofer, J.A.V.; Rohn, J.; Luo, J. The Performance of Geothermal Passive Heating and Cooling for Asphalt and Concrete Pavement. *Dev. Built Environ.* **2021**, *7*, 100051. [CrossRef]
22. Balbay, A.; Esen, M. Temperature Distributions in Pavement and Bridge Slabs Heated by Using Vertical Ground-Source Heat Pump Systems. *Acta Scientiarum. Technol.* **2013**, *35*, 677–685. [CrossRef]
23. Habibzadeh-Bigdarvish, O.; Yu, X.; Li, T.; Lei, G.; Banerjee, A.; Puppala, A.J. A Novel Full-Scale External Geothermal Heating System for Bridge Deck de-Icing. *Appl. Therm. Eng.* **2021**, *185*, 116365. [CrossRef]
24. Han, C.; Yu, X. (Bill) Feasibility of Geothermal Heat Exchanger Pile-Based Bridge Deck Snow Melting System: A Simulation Based Analysis. *Renew. Energy* **2017**, *101*, 214–224. [CrossRef]
25. Wang, H.; Chen, Z. Study of Critical Free-Area Ratio during the Snow-Melting Process on Pavement Using Low-Temperature Heating Fluids. *Energy Convers. Manag.* **2009**, *50*, 157–165. [CrossRef]
26. Mirzanamadi, R.; Hagentoft, C.E.; Johansson, P. Coupling a Hydronic Heating Pavement to a Horizontal Ground Heat Exchanger for Harvesting Solar Energy and Heating Road Surfaces. *Renew. Energy* **2020**, *147*, 447–463. [CrossRef]
27. Mirzanamadi, R.; Hagentoft, C.E.; Johansson, P. Numerical Investigation of Harvesting Solar Energy and Anti-Icing Road Surfaces Using a Hydronic Heating Pavement and Borehole Thermal Energy Storage. *Energies* **2018**, *11*, 3443. [CrossRef]
28. Guldentops, G.; Nejad, A.M.; Vuye, C.; Van den bergh, W.; Rahbar, N. Performance of a Pavement Solar Energy Collector: Model Development and Validation. *Appl. Energy* **2016**, *163*, 180–189. [CrossRef]
29. Nahvi, A.; Pyrialakou, V.D.; Anand, P.; Sadati, S.M.S.; Gkritza, K.; Ceylan, H.; Cetin, K.; Kim, S.; Gopalakrishnan, K.; Taylor, P.C. Integrated Stochastic Life Cycle Benefit Cost Analysis of Hydronically-Heated Apron Pavement System. *J. Clean. Prod.* **2019**, *224*, 994–1003. [CrossRef]
30. Chapman, W.P. Design of Snow Melting Systems. *Heat. Vent.* **1952**, *49*, 88–102.
31. Kilkis, I.B. Design of Embedded Snow-Melting Systems Part 1: Heat Requirements-an Overall Assessment and Recommendations. *ASHRAE Trans.* **1994**, *100*, 423–433.
32. Kilkis, I.B. Design of Embedded Snow-Melting Systems: Part 2, Heat Transfer in the Slab-a Simplified Model. *ASHRAE Trans.* **1994**, *100*, 434–441.
33. Rees, S.J.; Spitler, J.D.; Xiao, X. Transient Analysis of Snow-Melting System Performance. *ASHRAE Trans.* **2002**, *108*, 406–423.
34. Liu, X.; Rees, S.J.; Spitler, J.D. Modeling Snow Melting on Heated Pavement Surfaces. Part I: Model Development. *Appl. Therm. Eng.* **2007**, *27*, 1115–1124. [CrossRef]
35. Kayaci, N.; Demir, H. Numerical Modelling of Transient Soil Temperature Distribution for Horizontal Ground Heat Exchanger of Ground Source Heat Pump. *Geothermics* **2018**, *73*, 33–47. [CrossRef]
36. Lund, J.W. *Pavement Snow Melting*; Geo-Heat Center, Oregon Institute of Technology: Klamath Falls, OR, USA, 2000; pp. 12–19.
37. Xu, H.; Shi, H.; Tan, Y.; Ye, Q.; Liu, X. Modeling and Assessment of Operation Economic Benefits for Hydronic Snow Melting Pavement System. *Appl. Energy* **2022**, *326*, 119977. [CrossRef]
38. Pahud, D. *BRIDGESIM: Simulation Tool for the System Design of Bridge Heating for Ice Prevention with Solar Heat Stored in a Seasonal Ground Duct Store, User Manual*; SUPSI: Lugano, Switzerland, 2008.
39. Abbasi, M. Non-Skid Winter Road, Investigation of Deicing System by Considering Different Road Profiles. Ph.D. Thesis, Chalmers University of Technology, Gothenburg, Sweden, 2013.
40. Li, K.; Hong, N. Dynamic Heat Load Calculation of a Bridge Anti-Icing System. *Appl. Therm. Eng.* **2018**, *128*, 198–203. [CrossRef]
41. Rahman, M.L.; Malakooti, A.; Ceylan, H.; Kim, S.; Taylor, P.C. A Review of Electrically Conductive Concrete Heated Pavement System Technology: From the Laboratory to the Full-Scale Implementation. *Constr. Build. Mater.* **2022**, *329*, 127139. [CrossRef]
42. Jiao, W.; Sha, A.; Liu, Z.; Li, W.; Zhang, L.; Jiang, S. Optimization Design and Prediction of the Snow-Melting Pavement Based on Electrical-Thermal System. *Cold Reg. Sci. Technol.* **2022**, *193*, 103406. [CrossRef]
43. Liu, X.; Rees, S.J.; Spitler, J.D. Modeling Snow Melting on Heated Pavement Surfaces. Part II: Experimental Validation. *Appl. Therm. Eng.* **2007**, *27*, 1125–1131. [CrossRef]

44. Li, H.; Harvey, J.; Jones, D. Multi-Dimensional Transient Temperature Simulation and Back-Calculation for Thermal Properties of Building Materials. *Build. Environ.* **2013**, *59*, 501–516. [CrossRef]
45. Lai, J.; Qiu, J.; Chen, J.; Fan, H.; Wang, K. New Technology and Experimental Study on Snow-Melting Heated Pavement System in Tunnel Portal. *Adv. Mater. Sci. Eng.* **2015**, *2015*, 706536. [CrossRef]
46. Liu, K.; Huang, S.; Jin, C.; Xie, H.; Wang, F. Prediction Models of the Thermal Field on Ice-Snow Melting Pavement with Electric Heating Pipes. *Appl. Therm. Eng.* **2017**, *120*, 269–276. [CrossRef]
47. Liu, K.; Huang, S.; Xie, H.; Wang, F. Multi-Objective Optimization of the Design and Operation for Snow-Melting Pavement with Electric Heating Pipes. *Appl. Therm. Eng.* **2017**, *122*, 359–367. [CrossRef]
48. Liu, K.; Huang, S.; Wang, F.; Xie, H.; Lu, X. Energy Consumption and Utilization Rate Analysis of Automatically Snow-Melting System in Infrastructures by Thermal Simulation and Melting Experiments. *Cold Reg. Sci. Technol.* **2017**, *138*, 73–83. [CrossRef]
49. Kim, M.S.; Jang, D.U.; Hong, J.S.; Kim, T. Thermal Modeling of Railroad with Installed Snow Melting System. *Cold Reg. Sci. Technol.* **2015**, *109*, 18–27. [CrossRef]
50. Chapman, W.P.; Katunich, S. Heat Requirements of Snow Melting Systems. *ASHAE Trans.* **1956**, *62*, 359–372.
51. Ling, F.; Zhang, T. A Numerical Model for Surface Energy Balance and Thermal Regime of the Active Layer and Permafrost Containing Unfrozen Water. *Cold Reg. Sci. Technol.* **2004**, *38*, 1–15. [CrossRef]
52. Mei, V.C. Heat Transfer of Buried Pipe for Heat Pump Application. *J. Sol. Energy Eng.* **1991**, *113*, 51–55. [CrossRef]
53. Chiasson, A.D.; Smith, M.D.; Rees, S.J. A Model for Simulating the Performance of a Pavement Heating System as a Supplemental Heat Rejecter with Closed-Loop Ground-Source Heat Pump Systems. *J. Sol. Energy Eng. Trans. ASME* **2000**, *122*, 183–191. [CrossRef]
54. Liu, K.; Fu, C.; Xie, H.; Wang, F.; Wang, X.; Bai, H. Design of Electric Heat Pipe Embedding Schemes for Snow-Melting Pavement Based on Mechanical Properties in Cold Regions. *Cold Reg. Sci. Technol.* **2019**, *165*, 102806. [CrossRef]
55. Dansk El-Varme Industri (DEVI) Ground Application. Ice & Snow Melting. Available online: https://assets.danfoss.com/documents/89841/AB212486469821en-010101.pdf (accessed on 7 November 2022).
56. Zhu, X.; Zhang, Q.; Du, Z.; Wu, H.; Sun, Y. Snow-Melting Pavement Design Strategy with Electric Cable Heating System Balancing Snow Melting, Energy Conservation, and Mechanical Performance. *Resour. Conserv. Recycl.* **2022**, *177*, 105970. [CrossRef]
57. Sullivan, W.G.; Wicks, E.M.; Koelling, C.P. *Engineering Economy*, 16th ed.; Pearson: Upper Saddle River, NJ, USA, 2015.
58. Nowak, K.; Rabczak, S. Technical and Economic Analysis of the External Surface Heating System on the Example of a Car Park. *Energies* **2020**, *13*, 6530. [CrossRef]
59. Demir, H.; Koyun, A.; Temir, G. Heat Transfer of Horizontal Parallel Pipe Ground Heat Exchanger and Experimental Verification. *Appl. Therm. Eng.* **2009**, *29*, 224–233. [CrossRef]